Research Article Vol. 33, No. 13 / 30 Jun 2025 / Optics Express 28290
Optics EXPRESS

Dual-comb mid-infrared spectromicroscopy with photothermal fluorescence detection

GWENDYLAN A. TURNER,[1] DANIEL I. HERMAN,[2] ALEKSANDR RAZUMTCEV,[1] MARKUS MANGOLD,[2] MINGHE LI,[1] ZIYI CAO,[1] JIAYUE RONG,[1] CHARLES A. BOUMAN,[3] GREGERY BUZZARD,[4] AND GARTH J. SIMPSON[1,*]

[1]*Department of Chemistry, Purdue University, West Lafayette, IN 47907, USA*
[2]*IRsweep AG, Stäfa, 8712, Switzerland*
[3]*Department of Electrical and Computer Engineering, Purdue University, West Lafayette, IN 47907, USA*
[4]*Department of Mathematics, Purdue University, West Lafayette, IN 47907, USA*
[*]*gsimpson@purdue.edu*

Abstract: An approach is described for spectrally parallel hyperspectral mid-infrared imaging with spatial resolution dictated by fluorescence imaging. Quantum cascade laser (QCL)-based dual-comb mid-infrared spectroscopy enables the acquisition of infrared spectra at high speed (<1 millisecond) through the generation of optical beat patterns and radio-frequency detection. The high-speed nature of the spectral acquisition is shown to support spectral mapping in microscopy measurements. Direct detection of the transmitted infrared beam yields high signal-to-noise spectral information, but long infrared wavelengths impose low diffraction-limited spatial resolution. The use of fluorescence detected photothermal infrared (F-PTIR) imaging provides high spatial resolution tied directly to the integrated IR absorption. Computational imaging using a multi-agent consensus equilibrium (MACE) approach combines the high spatial resolution of F-PTIR and the high spectral information of dual-comb infrared transmission in a single optimized equilibrium hyperspectral data cube.

1. Introduction

Infrared spectroscopy is among the most powerful analytical tools for chemical fingerprinting and materials characterization. The working principle of dual-comb mid-infrared (DC-IR) utilizes a pair of broad-band infrared frequency combs with close but nonidentical comb repetition frequencies. Heterodyne detection and Fourier transformation of the dual-comb time-domain beat patterns (interferograms) allow recovery of infrared absorption spectra with microsecond time resolution. Difference frequency generation (DFG) in a nonlinear medium is widely used for the generation of individual infrared combs. However, the introduction and commercial availability of high-power mid-IR quantum cascade lasers (QCLs) [1] have aided successful generation of QCL-based optical frequency combs [2], and these advancements have resulted in the recent development of QCL-based dual comb spectrometers exhibiting sub-wavenumber fidelity [3]. DC-IR enables parallel detection across all IR wavelengths, suppressing 1/f noise from slow drift and removing Poynting vector walk associated with frequency-swept QCL sources. The fast acquisition rate of DC-IR spectrometers has enabled the time-resolved study of protein dynamics [4], the fast monitoring of biochemical processes [5], and molecular adsorption/desorption [6]. Additionally, several modalities of DC spectroscopy have been implemented, with research groups demonstrating DC spectroscopy via photoacoustic [7,8] and photothermal [9] detection.

The high temporal resolution of DC-IR spectroscopy supports the possibility of fast, chemically specific, mid-IR spectroscopic imaging. While proof-of-concept imaging has been explored using DFG-based DC-IR [10,11], QCL-based DC-IR imaging has not been demonstrated in the literature to date. Rapid advances in QCL sources have substantially improved the accessibility

#557991 https://doi.org/10.1364/OE.557991
Journal © 2025 Received 28 Feb 2025; revised 21 Apr 2025; accepted 21 Apr 2025; published 26 Jun 2025

Optics EXPRESS

of QCL comb technology and its integration into dual comb systems, with access to broader spectral ranges than those easily achievable with (DFG)-based DC-IR [12]. These advances in fast, broadband, and accessible sources have set the stage for expansion of DC-IR for the characterization of heterogeneous, complex systems in chemistry and biology. However, the relatively low spatial resolution inherent to infrared imaging remains a limiting barrier in practical applications.

Addressing the diffraction-limited resolution limit in far-field infrared chemical imaging remains an open challenge. A number of promising strategies based on computational imaging methods have been attempted. Assuming the point-spread function of the imaging system is known, deconvolution methods, such as Fourier self-deconvolution and total variation, can be employed to increase the spatial resolution of IR imaging systems [13–15]. However, implementation of classical deconvolution methods remains limited in accuracy due to experimental realities such as scattering, glare, and blur, particularly in imaging within thick or spatially structured samples that are routinely characterized in microscopy measurements [16]. Once lost, computational recovery of high frequency content in the presence of measurement noise is generally an ill-posed operation that requires an exceptionally high signal to noise ratio. Hence, a union between innovative approaches in instrumentation hardware design and purely computational strategies is needed to further push the boundaries of sub-diffraction hyperspectral imaging in the mid-IR range.

Optical photothermal infrared (O-PTIR) is a recent effort that addresses spatial resolution limitations of infrared imaging. O-PTIR uses an additional tightly focused visible laser beam to probe local temperature variations in the sample associated with infrared absorption. One of the most recent O-PTIR modalities, fluorescence-detected photothermal mid-infrared (F-PTIR) microscopy leverages the thermal sensitivity of the fluorescence quantum yield [17,18], which provides simpler PSFs and ~100-fold signal-to-noise ratio improvement as compared to previously established detection scheme based on refractive index modulation [17–22]. Following initial establishment, researchers have demonstrated further improvements and broad application ranges of F-PTIR microscopy [23–25]. Due to its high sensitivity and improved selectivity enabled by fluorescence labeling, F-PTIR is particularly promising as a potential modality for integration with dual-comb infrared sources.

In this work, we not only demonstrate QCL-based DC-IR imaging in the mid-IR range, but we also achieve hyperspectral high-resolution mid-IR microscopy through the integration of DC-IR dual comb source with a custom F-PTIR microscope. DC-IR was used for fast sample-scanning hyperspectral imaging with high spectral but low spatial resolution, while complementary photothermal microscopy provided high spatial resolution but spectrally broadband absorption maps. A multi-agent consensus equilibrium (MACE) algorithm for computational imaging was adapted for hyperspectral image reconstruction and used to merge the two imaging modalities [26–28]. The equilibrium output of MACE balanced the cost functions inherent within each of the two imaging methods (DC-IR and F-PTIR) to create a hyperspectral image cube with both high spatial and spectral resolution. The present proof-of-concept demonstration of DC-IR imaging coupled with MACE reconstruction opens new prospects for the development of fast hyperspectral imaging in the fingerprint region with high spatial, spectral, and temporal resolution.

2. Materials and methods

2.1. DC-FPTIR microscope

The dual comb F-PTIR microscope consisted of a commercially available QCL dual-comb spectroscopy (DCS) system (IRis-core, IRsweep, Switzerland) co-propagated with a 532 nm diode laser (LOCLasers -GL532) for fluorescence excitation. The IR and probe beams were combined using a germanium window (Thorlabs WG91050-G) and focused onto the sample plane with a ZnSe aspherical lens (Edmund Optics, 39-469).

Optics EXPRESS

The dual comb F-PTIR microscope consisted of a commercially available QCL dual-comb spectroscopy (DCS) system (IRis-core, IRsweep, Switzerland) co-propagated with a 532 nm diode laser (LOCLasers -GL532) for fluorescence excitation. The IR and probe beams were combined using a germanium window (Thorlabs WG91050-G) and focused onto the sample plane with a ZnSe aspherical lens (Edmund Optics, 39-469).

As illustrated in Fig. 1**,** IR transmission measurements of the DCS through the sample were accomplished with a pair of fast mid-infrared detectors (Vigo), with one serving as a reference detector located prior to the IR-visible beam combination and the other as a transmitted IR detector after the sample. The dual comb source was composed of two 7.5 GHz combs with a relative spacing that resulted in 200 spectral elements between 1035 cm^{-1} and 1085 cm^{-1}. For hyperspectral imaging, a piezoelectric scanning stage (MadCityLabs NanoBio 300) provided positional sample scanning across a 125 µm by 250 µm field of view (8100 pixels). Hyperspectral data were acquired through pixel-by-pixel high-speed digitization with a single pixel acquisition time of 260 microseconds. It is worth noting that the speed of hyperspectral image acquisition was limited not by infrared spectral scanning, but by digitization speed, delivering a total time of 40 seconds per image for all IR transmission images presented herein. A line-by-line digitization scheme presented in the supporting information was found to reduce total acquisition time to an acquisition time of 10 seconds, again limited by the computational requirements of the DC-IR image. Imaging at this speed also approached reasonable mechanical limits of the piezo stage, resulting in limited total range of the fast axis. Images and further discussion are presented in the Supplement 1.

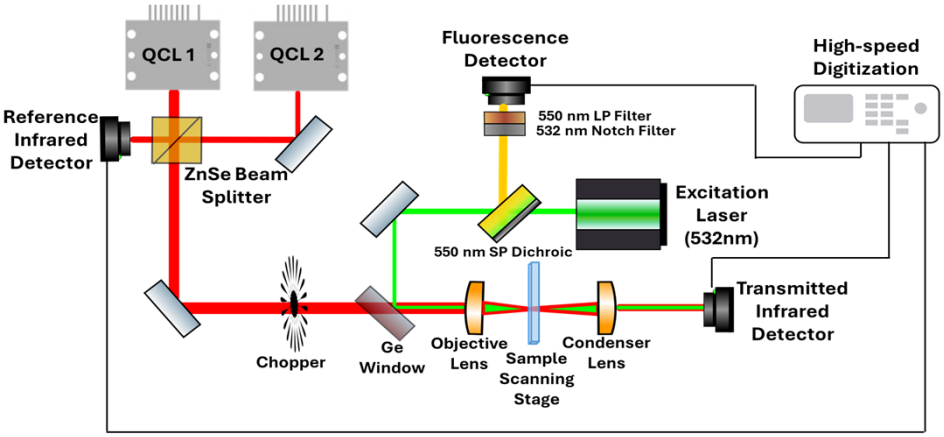

Fig. 1. Instrument schematic for DC-FPTIR and IR transmission measurements. A dual-comb QCL Source is combined with a 532 nm laser via a germanium window and focused onto the sample plane with a zinc selenide refractive objective. Fluorescence measured in the back-propagating (epi) direction using a short pass (SP) dichroic mirror, a notch filter at the visible laser excitation, and a 550 nm long pass (LP) filter.

Fluorescence signal was acquired with a photomultiplier tube (PMT) assembly in epi-detection (Hamamatsu H10721-210) where fluorescence was reflected to a 550 nm short-pass dichroic mirror (Thorlabs) and subsequently filtered using a 532 nm notch (Thorlabs), and a 550 nm (Thorlabs) long-pass filters. Fluorescence images were acquired with identical stage movement as used for the dual comb transmission images, with a pixel dwell time of 260 µs. The computational load of the fluorescence images was significantly reduced compared to the hyper-spectral DC-IR images, resulting in total acquisition times of a few seconds. For F-PTIR imaging, a chopper at a modulation frequency of 200 Hz was introduced into the IR beam path, and fluorescence was detected using a PMT. The sample was scanned through the same field of view with a total

Optics EXPRESS

acquisition time of 150 seconds per image, which corresponds to a pixel dwell time of 15 ms and represents three modulation periods of the chopper. The reference of the chopper was collected to transduce the modulated fluorescence image. Thus, the collected F-PTIR image represents the integrated photothermal modulation across the entire infrared range. Longer imaging times were required for F-PTIR imaging due to the relatively slow speed of the available chopper. F-PTIR imaging speed can be increased using faster modulation, and signal-to-noise can be improved with a reflective objective that ensures a focal overlap for the fluorescence and infrared beam.

2.2. Sample preparation and characterization

Hydrated rhodamine-6 G (R6 G) – associated silica gel samples were prepared through manual mortar-and-pestle grinding of silica gel and subsequent dissolution of silica gel and rhodamine 6-G in deionized water. The water was evaporated over 24 hours, and the remaining particles were placed onto a calcium fluoride (CaF_2) slide for imaging. Polydextran samples were prepared by dissolving rhodamine B-labeled polydextran (10,000 M.W., ThermoFischer Scientific) in deionized water, which was deposited onto a calcium fluoride slide and left to dry for 24 hours.

The transmitted infrared spectrum for silica gel spectra was compared to literature reference transmission spectrum [29]. DCS rhodamine-B labeled polydextran were compared to attenuated total reflectance spectra of the pure sample component taken with a Thermo Nicolet 6700 FT-IR.

2.3. Hyperspectral data fusion

A custom multi-agent consensus equilibrium (MACE) algorithm, implemented in-house in MATLAB, was employed to merge the hyperspectral DC-IR image cube with corresponding fluorescence and fluorescence-detected photothermal infrared (F-PTIR) measurements [30]. MACE provides a formal framework for balancing the reconstruction constraints of multiple imaging modalities [26–28,31,32], reconciling the high spectral but low spatial resolution of DC-IR data with the high spatial but low spectral resolution of F-PTIR measurements. The approach builds on foundational work in computational image reconstruction, with extensive prior descriptions available in the literature [26–28]. However, the implementation used in this study required substantial customization to accommodate the specific data structures and resolution disparities inherent to the imaging modalities.

In the MACE framework, each computational agent independently generates a candidate reconstruction of the object $\mathbf{X}_n$, evaluated within a common solution space. In this application, that space for each $\mathbf{X}_n$ is defined by a three-dimensional hyperspectral data cube with two spatial dimensions and one spectral dimension. For a given nth individual computational image reconstruction agent $\mathbf{F}_n$ operating on an input of $\mathbf{X}_n$, subject to constraints from measurements $\mathbf{Y}_n$, the optimized reconstructed output from just that individual agent is given by an updated $\mathbf{X}_n$. The collective state of all agents is represented as a single global vector $\mathbf{X}_{tot}$, formed by concatenating the individual reconstructions $\mathbf{X}_{tot} = [\mathbf{X}_1 \ldots \mathbf{X}_N]$. This global state $\mathbf{X}_{tot}$ is iteratively refined by applying a set of agent-specific update rules, which together define the global MACE operator. In the specific instance considered herein, equilibrium is evaluated between the reconstructions from two agents; one based on reconstruction of the hypercube from the photothermal fluorescence measurements $\mathbf{F}_{pt}$, and one based using the DC-IR transmission measurements as an input for the reconstruction $\mathbf{F}_{ir}$. The global operator $\mathbf{F}$ is formed by stacking these two agent operators in the MACE computation, as shown below.

$$\mathbf{F}\mathbf{X}_{tot} = \begin{pmatrix} \mathbf{F}_{pt}\mathbf{X}_{pt} \\ \mathbf{F}_{ir}\mathbf{X}_{ir} \end{pmatrix} \tag{1}$$

At this point, the two agents operate entirely independently, each serving to reconstruct its own hyperspectral datacube $\mathbf{X}_n$. To facilitate consensus, The individual agent operations are linked

Optics EXPRESS

through the broadcast mean operator $\mathbf{GX}_{tot}$, which generates as an output the arithmetic mean of all agents' state, broadcast as an array of the same dimensionality as $\mathbf{X}_{tot}$.

$$\mathbf{GX}_{tot} = \begin{pmatrix} \bar{\mathbf{X}} \\ \bar{\mathbf{X}} \end{pmatrix}; \bar{\mathbf{X}} = \tfrac{1}{2}[\mathbf{X}_{pt} + \mathbf{X}_{ir}] \tag{2}$$

The consensus equilibrium solution for $\mathbf{X}_{tot}$ arises when the operation $\mathbf{FX}_{tot}$ returns a vector of states equal to the result of the broadcast mean, as shown in Eq. (3) below.

$$\mathbf{FX}_{tot} = \mathbf{GX}_{tot} \tag{3}$$

Simple algebraic manipulation allows reformulation of the above equality to $2\mathbf{FX}_{tot} - \mathbf{X}_{tot} = 2\mathbf{GX}_{tot} - \mathbf{X}_{tot}$; which in turn leads to a useful definition of the operator **T,** such that $(2\mathbf{G} - \mathbf{I})(2\mathbf{F} - \mathbf{I})\mathbf{X}_{tot} \equiv \mathbf{TX}_{tot} \cong \mathbf{X}_{tot}$, with $\mathbf{T} \equiv (2\mathbf{G} - \mathbf{I})(2\mathbf{F} - \mathbf{I})$ as detailed previously [33]. Note that the expression $(2\mathbf{G} - \mathbf{I})$ is involutory, and thus is its own inverse, enabling this definition of **T** and providing a fixed-point formulation compatible with Mann iteration for map optimization [34].

In practice, the exact equilibrium conditions with $\mathbf{FX}_{tot} = \mathbf{GX}_{tot}$ (or equivalently, $\mathbf{TX}_{tot} = \mathbf{X}_{tot}$) is approached iteratively rather than solved directly, with iterations terminated after the difference between $\mathbf{FX}_{tot}$ and $\mathbf{GX}_{tot}$ falls between a preset tolerance. Each update for a given individual agent was evaluated using the gradient of the corresponding cost function, which in turn was defined as the squared norms between the observation $\mathbf{Y}_n$ for the nth agent and the forward model operation $\mathbf{A}_n$; $cost_n = ||\mathbf{Y}_n - \mathbf{A}_n\mathbf{X}_n||^2$. Computational details on the iterative procedure are summarized in the Supplement 1.

With this general framework in place, the specific agents for hypercube reconstruction from the transmitted DC-IR and F-PTIR observables can be considered. In the case of the DC-IR, the measured image retained high spectral resolution at all positions, but the long infrared wavelength (~10 μm) introduced a broad point-spread function (**psf**) and considerable spatial blur. This blur was modeled as the convolution of the **psf** with each frame in the hyperspectral cube, evaluated only in the spatial dimension. A specific cost function of $cost_{ir} = ||\mathbf{Y}_{ir} - \mathbf{psf}_{ir} \otimes \mathbf{X}_{ir}||^2$ was used to assess the quality of both a particular selection for the object from the infrared observables $\mathbf{X}_{ir}$ and the **psf** through comparison with the experimentally measured blurred hypercube $\mathbf{Y}_{ir}$. An initial estimate of the point spread function (**psf**) was determined by first performing Richardson-Lucy blind deconvolution of a representative frame in the hyperspectral data cube, then fitting the recovered **psf** to a symmetric Gaussian function. From this cost function, the derivative with respect to $\mathbf{X}_{ir}$ yields the following expression for the updated cube based on steepest descent along the negative gradient.

$$\mathbf{F}_{ir}(\mathbf{X}_{ir})_i = (\mathbf{X}_{ir})_i + \alpha\mathbf{psf}_{ir}^T \otimes (\mathbf{Y}_{ir} - \mathbf{psf}_{ir} \otimes (\mathbf{X}_{ir})_i) = \mathbf{T}(\mathbf{X}_{tot})_i \tag{4}$$

For a given input $(\mathbf{X}_{ir})_i$, the agent $\mathbf{F}_{ir}$ operates to produce an updated $\mathbf{X}_{ir}$ by progression along the negative gradient of the cost function. The expression in Eq. (4) can be simplified further by noting that $\mathbf{psf}^{\mathrm{T}} = \mathbf{psf}$ for a symmetric Gaussian blur filter. A scalar factor α was introduced to Eq. (4) to control the rate of convergence between the two agents in the MACE implementation, with $0 < \alpha \leq 1$.

For the photothermal image, there is a mismatch in dimensions between the 2D observations in $\mathbf{Y}_{pt}$ and the 3D hyperspectral object $\mathbf{X}_{pt}$; the measured photothermal response using an optical chopper integrates over all infrared wavelength channels. Mathematically, the integration operation can be performed by left-multiplication of the rank 3 tensor $\mathbf{X}_{pt}$ by a column vector of 1's along the wavelength axis and an identity matrix along the spatial dimensions, denoted by the tensor $\mathbf{A}_{pt}$. The corresponding cost function is given by $cost_{pt} = ||\mathbf{Y}_{pt} - \mathbf{A}_{pt}\mathbf{X}_{pt}||^2$. As in the

Optics EXPRESS

preceding case, the agent for the photothermal microscopy produces an updated $\mathbf{X}_{pt}$ based on progression along the negative gradient of the cost function.

$$\mathbf{F}_{pt}(\mathbf{X}_{pt})_i = (\mathbf{X}_{pt})_i + \alpha \mathbf{A}^T(\mathbf{Y}_{pt} - \mathbf{A}(\mathbf{X}_{pt})_i) = \mathbf{T}(\mathbf{X}_{tot})_i \tag{5}$$

In this case, the adjoint $\mathbf{A}^T$ is given by a row-vector of 1's in wavelength for back-expansion along the wavelength axis. Iterative optimization typically results in convergence within a few iterations (~10).

3. Results

3.1. DC-IR transmission hyperspectral imaging

Dual comb infrared transmission measurements are shown in Fig. 2 for a sample consisting of silica gel-particles infused with rhodamine-6 G fluorescent dye. The signal to noise ratio (SNR) within one pixel was noteworthy, with detectable changes of a few parts per 1000 in percent transmission. This SNR was achieved with a single pixel integration time of 260 µs for the DC-IR measurements and is consistent with prior reports for DC-IR [12]. The transmitted IR from a representative single pixel contains sharp features with a periodicity of ~5 cm^{-1}, which are attributed to etalon interference effects from the co-parallel planar surfaces of the CaF_2 substrate. Transmittance spectra were obtained following normalization by a featureless region within the field of view (top right corner).

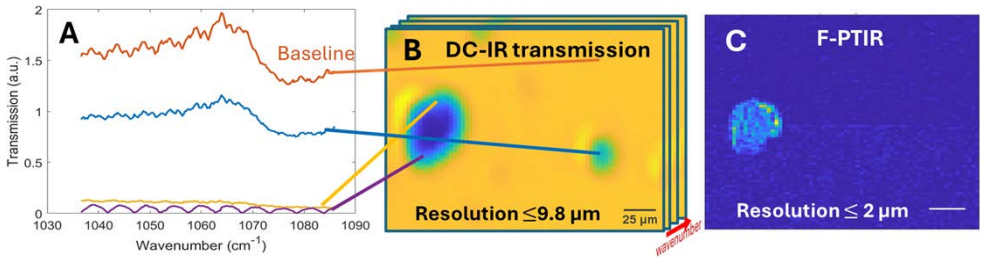

Fig. 2. Raw DC-IR hyperspectral image stack of R6G-associated silica gel particles and the corresponding F-PTIR image. (A) Representative single-pixel spectra of the transmitted DC-IR intensity. (B) Representative frame for a single infrared wavelength (1070 cm^{-1}). (C) F-PTIR micrograph of the same field of view. Resolution was estimated through the derivative of a line scan across the edge of the leftmost particle.

While the DC-IR measurements yield exquisite sensitivity in the spectral domain, the long wavelength inherent in IR spectroscopy results in relatively low spatial resolution. Cross-sectional analysis of the particles shown in Fig. 2(B) enabled estimation of the spatial resolution. Treating the particles as comprising sharp knife-edges, the resolution can be estimated directly from the derivative of a line-scan across the particle edge [35,36]. This approach provides a lower bound on the spatial resolution, yielding the correct spatial resolution only for particles exhibiting sharp edges with "flat-top" intensity profiles. Based on this analysis, the minimum resolvable distance of the DC-IR image of silica gel was found to be 9.8 µm. This value is less resolved than the diffraction-limited value of 5.7 µm, given by the numerical aperture (NA) of the aspherical lens (1.00) and the IR wavelength (1070cm^{-1}); however, the resolution reported below is prone to underestimate the resolution due to departures from flat-top profiles in infrared absorption. This value is well aligned with performances previously reported in DFG-based DC-IR microscopy [10,37]. The spatial resolution may suffer as a result of imperfect spatial overlap of the two combs at the sample plane. In either case, it is far below the spatial resolution routinely achieved in optical microscopy using visible light.

Optics EXPRESS

3.2. F-PTIR and fluorescence imaging

Fluorescence-detected photothermal infrared (F-PTIR) microscopy was performed to improve on the spatial resolution in infrared absorption microspectroscopy relative to direct IR transmission detection, the result of which is shown in Fig. 2(C). In F-PTIR, the IR absorption is transduced through a corresponding thermal modulation in the fluorescence intensity as shown in Fig. 1. This approach leverages a high intrinsic sensitivity of the fluorescence quantum efficiency with temperature, with many common fluorescent dyes yielding emission intensity reductions of 1-2%/^{o}C. Relative to direct detection of the transmitted IR, F-PTIR has the potential to yield substantial improvements in spatial resolution. Consistent with this expectation, spatial resolution in the F-PTIR image was limited by pixelation effects to <2 μm rather than from the optical point spread function.

Modulation of the dual-comb source using an optical chopper provided high modulation depths for F-PTIR detection, with all IR wavelengths within the emission bandwidth of the QCL pair contributing to the measured modulation in fluorescence. However, much of the detailed spectral information within the IR beam was lost in this manner, as the F-PTIR in this configuration integrated over the absorption measured simultaneously at all wavelengths within the QCL bandwidth. As such, F-PTIR yielded excellent spatial resolution but limited spectral information, in direct contrast to DC-IR measurements.

3.3. Computational merging with multi-agent consensus equilibrium (MACE)

The highly complementary information content from DC-IR and F-PTIR is well-suited for computational imaging methods for data fusion, the results of which are shown in Fig. 3 evaluated using MACE. In MACE, a balance is struck between the inherent cost structure within each agent, producing a net equilibrium output that, under favorable conditions, retains the features from which deviation is most costly. Both DC-IR and F-PTIR were cast as agents designed to output hyperspectral data cubes in a commonly shared hyperspectral "MACE-space". Details of the MACE implementation and simulation results using ground truth outcomes for algorithm characterization are summarized in the Supplement 1 and shown in Visualization 1. In brief, the spectral domain was constrained by blind non-negative matrix factorization (NMF). The hyperspectral response at each pixel was then generated from a linear combination of the two most probable pure component source spectra, recovered by NMF from analysis of the entire set of single-pixel absorbance spectra derived from the transmission hypercube depicted in Fig. 2(B). MACE evaluation was performed iteratively, requiring few (<10) iterations to converge to the most probable hyperspectral image $\hat{\mathbf{X}}$ consistent with both sets of observables. The two forward models employed in MACE consisted of: i) frame-wise spatial convolution of $\hat{\mathbf{X}}$ with a blurred point-spread function to conform to the hyperspectral IR absorption map derived from the IR transmission $\boldsymbol{y}_{\mathrm{IR}}$, and ii) integration over the spectral response in $\hat{\mathbf{X}}$ to recover the F-PTIR image $\mathbf{Y}_{\mathrm{FPTIR}}$. Prior to implementation of MACE with experimental data, simulations to assess the reliability of the algorithm were performed, the results of which are detailed in the Supplement 1.

Consistent with expectations for MACE, the reconstructed DC-F-PTIR hypercube retains both the high spatial resolution of F-PTIR and the high spectral resolution of DC-IR. Using the same knife-edge method described previously, the DC-F-PTIR hypercube exhibited a spatial resolution of <2 μm (compared to ~10 μm for DC-IR).

Notably, many of the oscillatory components in the spectra shown in Fig. 2 were absent from those same pixels in the reconstructed absorbance image from MACE. Much of the loss arose from the simple change from IR transmission to absorbance; oscillatory features shared across the field of view were removed upon normalizing by a blank region in the field of view to calculate the IR absorbance map. Interestingly, strong sinusoidal oscillations were still observed for the region in the heart of the silica gel particle on the left side of the field of view. These residual

Optics EXPRESS

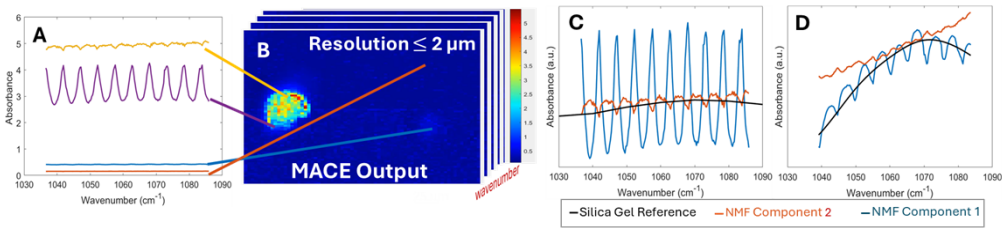

Fig. 3. Reconstructed hyperspectral data cube from MACE integration of F-PTIR and DC-IR images: (A) Representative single-pixel spectra from different locations. (B) Hyperspectral data cube from the equilibrium balance between IR absorption hyperspectral imaging and integrated photothermal microscopy. (C) The two basis-set spectral components produced by the reconstruction using non-negative matrix factorization, together with the absorbance spectrum of silica gel. (D) Similar comparison as in (C), but after digital smoothing of the two components to suppress etalon-like interferences.

oscillations are attributed to shifts in the etalon frequency from the additional thickness of the particle relative to the bare slide.

The spectral decomposition by NMF preceding MACE produced two source spectra shown in Fig. 3(C), from which the spectrum in every pixel in the reconstruction was derived. The data in Fig. 3(D) are identical to those in **3C**, following smoothing with a rolling average to minimize the sinusoidal amplitude. Good agreement is observed between the smoothed, baselined Component 1 spectrum and the previously reported absorbance spectrum of silica gel over the same spectral range [38], given by the solid black trace in Figs. 3(C) and 3(D). In contrast to Component 1, Component 2 exhibits a much flatter spectral response, with only minor amplitude changes across the IR tuning range. Similar features are also reflected in the raw single-pixel spectra shown in Fig. 3(A), in which one of the brightest regions for F-PTIR yielded a high and spectrally flat absorbance. These featureless regions are tentatively attributed to regions of high optical attenuation. Locations with sufficient optical density to effectively attenuate all the detectable transmitted IR will be characterized by flat, featureless absorbance spectra set by the negative log of the lowest detectable transmittance experimentally accessible by the instrument. The nonzero positive slope is tentatively attributed to a subtle wavelength dependence in this lower limit of detection, potentially arising from a combination of differences in detector sensitivity, IR laser fluence / stability, and wavelength-dependent dispersion in the optics dictating the throughput of the instrument and substrate.

While the F-PTIR measurements provide a rigorous bridge between connecting the infrared absorption with high-resolution fluorescence microscopy, any high-resolution contrast mechanism could aid in improving the resolution of the MACE algorithm's reconstructed outputs. To test this conjecture, additional MACE calculations were performed to computationally merge high-resolution fluorescence micrographs with low spatial resolution, high spectral resolution DC-IR images, the results of which are shown in Fig. 4 for rhodamine-B-labeled polydextran conglomerate particles. Despite the absence of a clear dependence of the fluorescence image on IR absorption, the high-resolution fluorescence micrograph nevertheless serves as an effective guide-star in the IR spatial deconvolution operation within the MACE algorithm. After MACE, the minimum resolvable distance was improved from 8.4 µm for DC-IR to 3.8 µm calculated using the same knife-edge approach detailed above.

These results suggest analogous potential benefits from integration of other high-resolution measurements, including bright-field images. These trends are in good qualitative agreement with prior hyperspectral IR imaging studies by Phal *et al.* [39]. In that work, computational reconstruction of infrared transmission hyperspectral images resulted in resolution at long

Optics EXPRESS

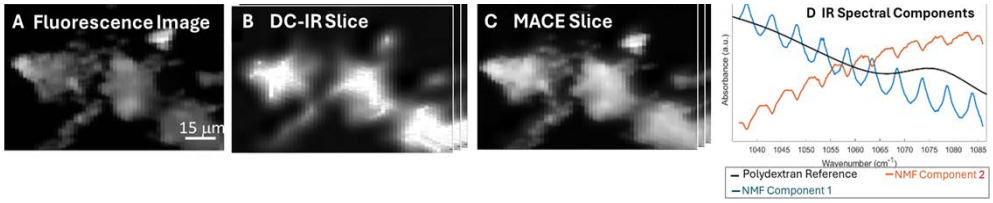

Fig. 4. (A) High-resolution fluorescence image of rhodamine-B (RhB)-labeled polydextran particles. (B) Representative spectral frame in a transmission DC-IR image stack. (C) Identical spectral frame following computational image reconstruction by MACE. (D) MACE spectral components (orange, blue) recovered by blind non-negative matrix factorization overlayed with the attenuated total reflection spectrum of RhB-labeled polydextran (black).

infrared wavelengths effectively set by the contrast from the shortest wavelength windows in the hyperspectral image cube. However, the visible probe beam used in F-PTIR and fluorescence microscopy is an order of magnitude shorter in wavelength than the blue edge of the infrared spectral window used in the previous hyperspectral IR imaging work, corresponding to substantial improvements in spatial resolution.

The recovered spectral components for the polydextran particles shown in Fig. 4(D) bear interesting similarities and differences with the spectra for silica gel particles in Fig. 3(D). For the polydextran, the more prominent Component 1 recovers a clear sinusoidal modulation present for the spectrally-modulated measurements, in excellent agreement with the results for Component 1 from silica gel. In this case, the baseline slope decreases in absorbance with increasing wavenumber, again in good agreement with the experimental absorbance spectrum of the analyte (in this case, polydextran) over the same spectral range. The absence of the peak shoulder at 1075 cm^{-1} could be attributed to slight miscalibration in the dual comb source, low transmission sensitivity when compared to sinusoidal interference effects, or slight shifts in the attenuated total reflection spectrum of polydextran. Interestingly, the smaller Component 2 is similar in both shape and baseline slope for both sets of images. These similar results across both samples are consistent with the prior attribution of Component 2 to a spectrum dominated by system noise following the absorption of all detectable IR transmittance (absorbance >~4). In both cases, the system noise is reasonably expected to be similar run-to-run, yielding similar featureless spectral responses for the corresponding spectral components, in excellent agreement with experimental observations.

4. Discussion

Instrumentation and computational methods are described to enable DC-IR hyperspectral imaging with spatial resolution below the infrared diffraction limit. These initial proof-of-concept results set the stage for a broad suite of applications in biology and materials analysis of heterogeneous assemblies. To our knowledge, these results represent the first demonstration of QCL-based DC-IR imaging in the vibrational "fingerprint" spectral range between ~500 cm^{-1} to ~1500 cm^{-1}. Additionally, MACE was realized as a tool for computational merging of hyperspectral infrared image cubes with either photothermal or fluorescence images. Both MACE outputs yielded spatial resolutions substantially higher than the calculated diffraction limits for the mid-infrared wavelengths utilized here. Computational integration of DC-IR hyperspectral imaging with F-PTIR allowed localization of the IR absorption with sub-diffraction limited spatial resolution and negligible loss in spectral accuracy. These collective results demonstrate a pathway to enable QCL-based DC-IR microscopy with high spatial resolution and rich hyperspectral information in the fingerprint IR spectral range.

Optics EXPRESS

In principle, photothermal fluorescence detection at radio frequencies characteristic of the QCL dual-comb system could chemically inform on the local environment immediately adjacent to the fluorescence reporter, enabling co-localization analysis over distances shorter even than the visible diffraction limit. Frequencies in the megahertz regime would correspond to colocalization distances on the order of nanometers, which represents a future opportunity for photothermal fluorescence spectroscopy. Such capability hinges on compatible thermal relaxation of the system. In the samples discussed herein, it is likely that the broad absorption throughout the spectral range paired with slow heat diffusivity relative to the comb frequency resulted in thermal "pile-up" that hindered photothermal detection. There is a potential avenue in addressing these challenges using tunable other dual-comb sources [40] and sample systems.

Funding. National Science Foundation (CHE-2004046, CHE-2305178, CHE-2320751); IRsweep AG.

Acknowledgement. This work was also supported in part by the Research Instrumentation Center in the Department of Chemistry at Purdue University.

Disclosures. Daniel Herman and Markus Mangold were employed by IRSweep AG at the time of measurements. The remaining authors declare no conflicts of interest.

Data Availability. All scripts used for processing and computational merging are available in [30]. Data are available upon request.

Supplemental document. See Supplement 1 for supporting content.

References

1. J. Faist, F. Capasso, D. L. Sivco, *et al.*, "Quantum Cascade Laser," Science **264**(5158), 553–556 (1994).
2. A. Hugi, G. Villares, S. Blaser, *et al.*, "Mid-infrared frequency comb based on a quantum cascade laser," Nature **492**(7428), 229–233 (2012).
3. M. Lepère, O. Browet, J. Clément, *et al.*, "A mid-infrared dual-comb spectrometer in step-sweep mode for high-resolution molecular spectroscopy," J. Quant. Spectrosc. Radiat. Transfer **287**, 108239 (2022).
4. L. Schubert, P. Langner, D. Ehrenberg, *et al.*, "Protein conformational changes and protonation dynamics probed by a single shot using quantum-cascade-laser-based IR spectroscopy," J. Chem. Phys. **156**(20), 204201 (2022).
5. M. J. Norahan, R. Horvath, N. Woitzik, *et al.*, "Microsecond-Resolved Infrared Spectroscopy on Nonrepetitive Protein Reactions by Applying Caged Compounds and Quantum Cascade Laser Frequency Combs," Anal. Chem. **93**(17), 6779–6783 (2021).
6. E. Lins, S. Read, B. Unni, *et al.*, "Microsecond Resolved Infrared Spectroelectrochemistry Using Dual Frequency Comb IR Lasers," Anal. Chem. **92**(9), 6241–6244 (2020).
7. J. T. Friedlein, E. Baumann, K. A. Briggman, *et al.*, "Dual-comb photoacoustic spectroscopy," Nat. Commun. **11**(1), 3152 (2020).
8. T. Wildi, T. Voumard, V. Brasch, *et al.*, "Photo-acoustic dual-frequency comb spectroscopy," Nat. Commun. **11**(1), 4164 (2020).
9. Q. Wang, Z. Wang, H. Zhang, *et al.*, "Dual-comb photothermal spectroscopy," Nat. Commun. **13**(1), 1–7 (2022).
10. P. Chang, N. Hoghooghi, S. Swartz, *et al.*, "Mid-Infrared Hyperspectral Microscopy with Broadband 1-GHz Dual-Comb Spectroscopy," *CLEO 2023* paper SM3O.2 SM3O.2 (2023).
11. H. Timmers, A. Kowligy, A. J. Lind, *et al.*, "Hyperspectral Microscopy with Broadband Infrared Frequency Combs," in *Conference on Lasers and Electro-Optics* (OSA, 2019), p. SF1E.4.
12. G. Ycas, F. R. Giorgetta, E. Baumann, *et al.*, "High-coherence mid-infrared dual-comb spectroscopy spanning 2.6 to 5.2 μm," Nat. Photonics **12**(4), 202–208 (2018).
13. P. Lasch and D. Naumann, "Spatial resolution in infrared microspectroscopic imaging of tissues," Biochim. Biophys. Acta, Biomembr. **1758**(7), 814 (2006).
14. T. P. Wrobel and R. Bhargava, "Infrared Spectroscopic Imaging Advances as an Analytical Technology for Biomedical Sciences HHS Public Access," Anal. Chem. **90**(3), 1444–1463 (2018).
15. F. Lai, J. Kandukuri, B. Yuan, *et al.*, "Thermal Image Enhancement through the Deconvolution Methods for Low-Cost Infrared Cameras," (n.d.).
16. M. Makarkin and D. Bratashov, "State-of-the-Art Approaches for Image Deconvolution Problems, including Modern Deep Learning Architectures," Micromachines **12**(12), 1558 (2021).
17. I. M. Pavlovetc, E. A. Podshivaylov, R. Chatterjee, *et al.*, "Infrared photothermal heterodyne imaging: Contrast mechanism and detection limits," J. Appl. Phys. **127**(16), 165101 (2020).
18. J. Yin, M. Zhang, Y. Tan, *et al.*, "Video-rate mid-infrared photothermal imaging by single-pulse photothermal detection per pixel," Sci. Adv. **9**(24), eadg8814 (2023).
19. M. S. Ünlü, J. X. Cheng, J. H. Connor, *et al.*, "Vibrational spectroscopic detection of a single virus by mid-infrared photothermal microscopy," Anal. Chem. **93**(8), 4100–4107 (2021).

Optics EXPRESS

20. V. Beltran, A. Marchetti, G. Nuyts, *et al.*, "Nanoscale Analysis of Historical Paintings by Means of O-PTIR Spectroscopy: The Identification of the Organic Particles in L′Arlésienne (Portrait of Madame Ginoux) by Van Gogh," Angew. Chem. Int. Ed. **60**(42), 22753–22760 (2021).
21. J. Yin, L. Lan, Y. Zhang, *et al.*, "Nanosecond-resolution photothermal dynamic imaging via MHZ digitization and match filtering," Nat. Commun. **12**(1), 7097 (2021).
22. Y. Su, X. Hu, H. Tang, *et al.*, "Steam disinfection releases micro(nano)plastics from silicone-rubber baby teats as examined by optical photothermal infrared microspectroscopy," Nat. Nanotechnol. **17**(1), 76–85 (2022).
23. A. Razumtcev, M. Li, J. Rong, *et al.*, "Label-Free Autofluorescence-Detected Mid-Infrared Photothermal Microscopy of Pharmaceutical Materials," Anal. Chem. **94**(17), 6512–6520 (2022).
24. D. Jia, Y. Zhang, Q. Yang, *et al.*, "3D Chemical Imaging by Fluorescence-detected Mid-Infrared Photothermal Fourier Light Field Microscopy," Chem. Biomed. Imaging **1**(3), 260–267 (2023).
25. A. Razumtcev, M. Li, and G. J. Simpson, "Parts-per-Million Detection of Trace Crystal Forms Using AF-PTIR Microscopy," Anal. Chem. **94**(38), 13100–13107 (2022).
26. G. T. Buzzard, S. H. Chan, S. Sreehari, *et al.*, "Plug-and-Play Unplugged: Optimization-Free Reconstruction Using Consensus Equilibrium," SIAM J. Imaging Sci. **11**(3), 2001–2020 (2018).
27. E. J. Reid, L. F. Drummy, C. A. Bouman, *et al.*, "Multi-Resolution Data Fusion for Super Resolution Imaging," IEEE Trans. Comput. Imaging **8**, 81–95 (2022).
28. S. Majee, T. Balke, C. Kemp, *et al.*, "Multi-Slice Fusion for Sparse-View and Limited-Angle 4D CT Reconstruction," IEEE Trans. Comput. Imaging **7**, 448–462 (2021).
29. R. M. Almeida and A. C. Marques, "Characterization of sol-gel materials by infrared spectroscopy," Handbook of Sol-Gel Science and Technology: Processing, Characterization and Applications 1121–1151 (2018).
30. "Simpson-Laboratory-for-Nonlinear-Optics/Dual-Comb-Photothermal-MACE," Github 2025 https://github.itap.purdue.edu/Simpson-Laboratory-for-Nonlinear-Optics/Dual-Comb-Photothermal-MACE.
31. V. Sridhar, X. Wang, G. T. Buzzard, *et al.*, "Distributed Iterative CT Reconstruction Using Multi-Agent Consensus Equilibrium," IEEE Trans. Comput Imaging **6**, 1153–1166 (2020).
32. X. Wang, V. Sridhar, Z. Ronaghi, *et al.*, "Consensus equilibrium framework for super-resolution and extreme-scale CT reconstruction," *International Conference for High Performance Computing, Networking, Storage and Analysis, SC* (2019).
33. J. R. W. Ulcickas, Z. Cao, J. Rong, *et al.*, "Multiagent Consensus Equilibrium in Molecular Structure Determination," J. Phys. Chem. A **124**(43), 9105–9112 (2020).
34. W. R. Mann, "Mean value methods in iteration," Proc. Am. Math. Soc. **4**(3), 506–510 (1953).
35. J. B. Pawley, *Handbook of Biological Confocal Microscopy* (Kluwer Academic Publishers, 1995).
36. A. Egner, S. Jakobs, and S. W. Hell, "Fast 100-nm resolution three-dimensional microscope reveals structural plasticity of mitochondria in live yeast," Proc. Natl. Acad. Sci. U. S. A. **99**(6), 3370–3375 (2002).
37. H. Timmers, A. Kowligy, A. J. Lind, *et al.*, "Hyperspectral Microscopy with Broadband Infrared Frequency Combs," *Conference on Lasers and Electro-Optics* SF1E.4 (2019).
38. R. M. Almeida and A. C. Marques, "Characterization of Sol–Gel Materials by Infrared Spectroscopy," in *Handbook of Sol-Gel Science and Technology* (Springer, Cham, 2016), pp. 1–31.
39. Y. Phal, L. Pfister, P. S. Carney, *et al.*, "Resolution Limit in Infrared Chemical Imaging," J. Phys. Chem. C **126**(23), 9777–9783 (2022).
40. P. Chang, R. Ishrak, N. Hoghooghi, *et al.*, "Mid-infrared hyperspectral microscopy with broadband 1-GHz dual frequency combs," APL Photonics **9**(10), 106111 (2024).